A. Butt[1], A. Hedayat[1], and O. Moradian[1,2]

[1] Department of Civil and Environmental Engineering, Colorado School of Mines, Golden, CO, USA.

[2]Department of Earth Sciences, Swiss Federal Institute of Technology (ETH), Zurich, Switzerland.

Corresponding author: Awais Butt (ambutt@mines.edu)

Key Points:

- Moment tensor inversion of acoustic emissions during viscosity and toughness dominated hydraulic fracturing showed tensile dominant fractures
- Higher b-values were observed for toughness compared to viscosity dominated propagation regimes
- The released seismic energy (number of AE events and the highest-magnitude event) was greater for the viscosity dominated fracturing
-

Abstract

While hydraulic fracturing (HF) is a widely employed process, the underlying fracturing processes are not clearly understood. Laboratory HF experiments with seismic monitoring can help with better understanding of the relationship between the generated HF network and the induced microseismicity while taking into account the effect of different HF parameters (injection fluid type and rate, stress conditions). In this study, HF experiments were performed on true-triaxially loaded Barre granite cubes, with real-time microseismic monitoring, to identify and characterize the stimulation processes associated with the viscosity and toughness dominated HF propagation regimes. Water and gear oil were used as the fracturing fluids. Moment tensor inversion technique was employed to determine the fracture mechanisms (tensile, shear, or mixed-mode). Viscosity propagation regime experiments involved higher breakdown pressures and larger injection fluid volumes relative to toughness propagation regime experiments. The microseismicity from toughness propagation regime experiments resulted in slightly larger b-value (2.25 compared to 2), indicating higher percentage of small magnitude events. The spatio-temporal evolution of fracture mechanisms indicated very dominant tensile fracturing (82-85%) during fracture initiation phase surrounding the injection region. As the fracture propagated away from the injection borehole, the number of shear and mixed-mode fracturing events increased. Overall, tensile fractures were dominant in both propagation regimes (ranging from 52% to 58%), which can be attributed maily to the absence of significant pre-existing faults/discontinuities in the very low permeability granite rock.

Plain Language Summary

HF has been employed to increase the permeability of deep energy reservoirs in crystalline granitic rocks and examples include enhanced geothermal systems. Different operational parameters such as the injection fluid type, injection rate, and stress conditions can significantly impact this rock stimulation and it is important to characterize this fracturing to estimate the efficiency of the HF process. This study involved laboratory HF of cubic Barre granite rock specimens with continuous microseismic monitoring using two different injection fluids. The experiments performed with higher viscosity injection fluid resulted in higher failure pressure and required a larger fluid volume, relative to experiments with low viscosity injection fluid. For all the experiments, majority of the identified fracturing involved generation of opening (tensile) fractures, particularly close to the fluid injection point. Experiment conducted with low viscosity injection fluid generated slightly larger number of low energy microseismic events. These results indicate that for very tight rocks with minimum pre-exisitng flaws, the majority of damage involves opening of new fractures, irrespective of the injection fluid. However, as the fracture size and parameter increase, the HF will follow the path of least resistance and will be a combination of opening and sliding (shear) fractures.

1 Introduction

Hydraulic stimulation techniques have been used over the past many decades to increase the permeability of sedimentary reservoir rocks for oil and gas production (Merrill & Schizer, 2013). This technique has also been utilized for many other applications, including, rock burst mitigation, carbon sequestration, tunnel and dam construction, water well development, etc. (Adams & Rowe, 2013). In recent years, the number of HF applications in hard crystalline rocks have increased considerably, of which an example can be enhanced geothermal system (EGS). In EGS, HF is used to stimulate and increase the permeability of an unconventional reservoir for cost-effective heat extraction (Olasolo et al. 2016). Stimulation of these hard crystalline rocks, at great depth (upto 5 km), is not a trivial task and few geothermal pilot projects had to be suspended due to large-magnitude seismicity experienced during the fluid injection phase of the operation (Zang & Stephansson, 2019). Although significant research efforts have been made to understand reservoir geomechanics, their focus has been HF in sedimentary rocks. The granitic rocks can be quite different from the traditional sedimentary reservoir rocks, due to their variable mineral composition and very low permeability (usually below 1%), relative to fractured or porous petroleum reservoir formations (Zhuang & Zang, 2021). Understanding the evolution of HF initiation and propagation in crystalline granitic rocks, the underlying fracture mechanisms, and their relationship to different injection parameters can be crucial for the successful implementation and overall optimization of deep underground stimulation operation.

Seismic monitoring, or acoustic emission (AE) monitoring at the laboratory scale, has been successfully used to monitor the initiation and propagation of laboratory HF in brittle rocks (Lockner, 1993; Stanchits et al., 2014). Seismic

monitoring can assist not only to map the propagating HF but also to understand the underlying damage mechanisms of the generated fracture network, which can significantly influence the efficient recovery of resources (Maxwell, 2014). This non-destructive monitoring technique has been extensively used in the laboratory to monitor the HF propagation in granite rock specimens. Some early work by Solberg et al. (1980) included HF experiments using water (viscosity – 1 cP) injection in westerly granite cylinders, at different injection rates (0.18-1.8 ml/min) and differential confining stresses (100- 300 MPa). The macroscopic fracture obtained due to pressurized fluid injection was tensile for rapid injection rates and low differential stresses. These experiments were monitored by six piezoelectric AE sensors and the cases with tensile macro-fractures were characterized by having no precursory AE activity and only a sudden burst of AEs as the fracture propagated through the specimens. Diaz et al. (2018), Zhuang et al. (2019a,b), Zhuang et al. (2020), and Jung et al. (2021) conducted HF experiments using water in cylindrical granite specimens (50 mm diameter / 100 mm length) with six AE sensors for acoustic monitoring. Overall, the maximum AE amplitude was found to be decreasing with the decreasing injection rate and cyclic injection schemes resulted in lower released AE energy and smaller aperture fractures. Apart from the basic AE analysis (amplitude, rate, cumulative AEs), Diaz et al. (2018) also determined the AE source locations and crack mechanisms. For crack classification as tensile or shear, average frequency (AF) / rise angle (RA) method (RILEM technical committee, 2010) was utilized, where rise angle is the relation between rise time and the maximum amplitude. Almost all the detected AE events (~97%) were determined to be tensile fractures, both for continuous and cyclic injection schemes. While important information has been revealed from these contributions, the results from small size cylindrical specimens, with pseudo triaxial confining state, and limited acoustic monitoring and analysis, may not present an elaborate picture of fracture propagation and the involved mechanisms as experienced by high strength granite at the field scale (Cheng & Zhang, 2020).

The subsurface rock strata are located in 3D stress conditions and experiments performed on cubic or cuboid rock specimens, loaded in all three mutually perpendicular directions, can present a better picture for understanding the mechanics of rock fracture (King et al., 2012). Limited number of studies exist which involve laboratory HF of relatively large cubical granite specimens with true-triaxial loading and extensive microseismic monitoirng. Mao et al. (2017) conduced HF experiments in large Luhui granite specimens (1000 x 1000 x 1000 mm) through water injection at 10 ml/min and with 32 channel AE measurement system. Limited AE analysis involved determination of crack mechanisms through AF/RA method, where shear fractures were found to be dominant. Ishida and company (Inui et al., 2014; Ishida 2001; Ishida et al., 2004; Ishida et al., 2012; Ishida et al., 2016) have performed HF experiments in Kurokamijima granite (dimension of 170 or 190 mm, each side of the block) with different viscosity injection fluids (transmission oil - 80 cP and ultra low viscosity CO_2 - 0.05 cP). The acoustic monitoring was performed using different configuration

of AE sensors ranging in number from 9 to 16 sensors. The AE analysis involved determination of the AE events locations and their source mechanisms through fault-plane solution. Fault-plane solution involves picking the polarity of the first motion of every single waveforms and is more reliable than the AF/RA method (Zang et al. 1998). It was concluded from these experiments that high viscosity injection tend to create thick and planar fractures, whereas, as the viscosity of the injection fluid decreases, the fracture extends more three dimensionally with multiple branches and complex fracture geometry. The determined fracture source mechanisms pointed towards a shear dominated fracturing, as the viscosity of injection fluid was reduced. However, the percentage of AE events that could be analyzed for source mechanisms was very small (<5% in some cases) and therefore might not completely be representative of the overall HF propagation mechanisms. Xing et al. (2019) and Hu et al. (2020) carried out HF experiments using water injection at 2 ml/min in ~300 x 300 x 300 mm cubic specimens of Luhui and Sierra White granite, respectively. Fault-plane solution method was utilized by both these studies to determine the mechanisms of fluid induced fractures, where shear fractures were found to be dominating in both these studies.

Moment tensor inversion is a quantitative approach which provides information about the motion at the seismic source and also the associated change in volume. It has been used widely in seismology, particularly for applications involving large non-DC component (Graham et al., 2010). The moment tensor analysis (MTA) technique has been utilized in only a handful of laboratory HF experimental studies involving granitic rocks. Li & Einstein (2019) conducted laboratory HF experiments on relatively small Barre granite prismatic cubes (76 x 152 x 25 mm), with a pre-existing vertical flaw, utilizing low viscosity injection fluid (3.89 cP) at two different injection rates (1.14 and 23.4 ml/min). Acoustic monitoring involved eight sensors from the MISTRAS group and through MTA, the source mechanisms were determined to be shear dominated for high injection rate and tensile dominated for low injection rates. Yamamoto et al. (2019) performed HF experiments with low viscosity injection fluid (0.8 cP) and rate (2 ml/min), on prismatic specimens of Kurokami–jima granite (85 mm $\times$ 170 mm $\times$ 85 mm). AE monitoring was performed with 16 sensors and MTA was used to determine the individual fracture mechanisms. Tensile and shear fracturing events were found to be dominating for the cases where rift (weakest) plane of granite was perpendicular and parallel to the fracture propagation direction, respectively. However, both above studies involved only a small vertical uniaxial loading (3-5 MPa) with no lateral confinement. Hampton et al. (2018) conduced HF experiments on true-triaxially loaded South Dakota granite specimens (150 x 150 x 250 mm) using a high viscosity gear oil at a low injection rate of 0.1 ml/min. AEs were recorded by 11 sensors where majority of AE events from were determined to tensile (70.5 %) through the MTA. However, these AE events were found to be randomly distributed all over the specimen and it was difficult to distinguish between the main HF and the non-hydraulically connected damage in the specimen. In addition to being small in numbers, these

studies did not provide the complete evolution of the HF and the underlying source mechanisms, from initiation till breakdown of the laboratory specimens.

While few HF studies in granitic rocks have attempted to explore the relationship between injection parameters (injection fluid viscosity / rate) and the detailed attributes of the detected microseismicity, it is imperative to know the fracturing state, that a particular selection of injection parameters in the laboratory experiments, will represent at the field-scale. However, nearly all of the existing studies have ignored this relationship, which is important to make the appropriate connection between the drastically different lab and field scales. In the field, the HF propagation transitions between different fracturing states represented by the various dominating propagation regimes involving different competing physical processes. If the energy consumed in the creation of new fracture surfaces is small relative to the viscous dissipation energy, viscous propagation regime (VPR) is the dominant regime. In toughness propagation regime (TPR), the energy spent on new fracture surface creation is much larger than the viscous counterpart (Detournay, 2004). For an impermeable material, the HF propagation can occur in either the VPR or TPR, depending on the variety of factors including the injection fluid properties (rate and viscosity), properties of rocks and the far field stresses (Sarmadivaleh, 2012). HF propagation in most of the field stimulation operations occurs in the VPR (Detournay, 2016); however, with the recent increase in utilizing very low viscosity injection fluid (e.g. liquid or supercritical CO_2), the HF propagation regime could transition to the TPR (Huang et al. 2019). Understanding the characteristics of the generated HF for situations involving different propagation regimes can be crucial to derive appropriate estimations for an efficient HF design.

In this study, laboratory HF experiments were performed in Barre granite cubes loaded true-triaxially with real-time microseismic and borehole pressure monitoring. The main objective of this study was to evaluate the spatio-temporal evolution of the generated HF network through the associated microseismicity following different propagation regimes. AE source localization and MTA was used to map and determine the fracturing mechanisms or modes of the detected AE events. The study focused on highlighting the evolution of dominant fracturing mechanisms throughout the stimulated rock volume at different stages of HF propagation.

2 Experimental setup and methodology

2.1 Material and borehole installation

HF was investigated using precisely cut and polished Barre granite cubes (165 mm x 165 mm x 165 mm) which represents the typical reservoir rocks encountered in geothermal projects (Cornet et al., 2007; McClure and Horne, 2014a; Xie et al., 2015). This medium-grained granite cubes, with mineral grain size between 0.25 and 3 mm, were all acquired from the same block extracted from E. L. Smith quarry located in the city of Barre, Vermont, USA (Dai et al. 2013). Feldspar is the main constituent mineral (65% by volume), followed by quartz

(25% by volume) and biotite (6% by volume) (Dai & Xia, 2013; Xia et al., 2008). Like most granites, Barre granite has a clear anisotropy with three mutually perpendicular cleavages, with different strength and densities of micro-cracks and minerals. These planes of weaknesses can be identified by obtaining the compressional (P-) wave velocities in the three different directions. The ultrasonic waveforms were acquired at multiple points on each side for all tested Barre granite cubic specimens before drilling the borehole for fluid injection experiments. Figure 1 (b) presents the ultrasonic waveforms acquired from different sides for the three Barre granite cubes utilized for the experiments in this study. The arrival time was determined manually for each acquired waveform and wave velocity was calculated. It can be observed from Figure 1(b) that the velocity was almost the same for different specimens in specific directions and were found to be ~4500 m/s (highest), ~4000 m/s (intermediate), and ~3500 m/s (slowest) , along the three planes which were termed as the hardway, grain, and rift plane, respectively. These velocity values, determined for different cubes, were very similar to what researchers have obtained in the previous studies involving Barre granite (Dai et al., 2013; Dai & Xia, 2013; Sano et al., 1992). Table 1 list different properties of Barre granite from the literature, where the lower limit was attributed to the rift plane of the Barre granite specimens.

Table 1. Properties of Barre granite from the literature

Density	2.65 gm/cm^3	Nur & Simmons (1969)
Porosity	0.006 ± 0.002	
Unconfined compressive strength	170-190 MPa	Miller (2008)
Tensile strength	10-15 MPa	Dai & Xia (2010) Li & Einstein (2019)
Mode-I fracture toughness	1.14-1.89 MPa. $(m)^{1/2}$	Nasseri et al. (2006) Sano et al. (1992)
Modulus of Elasticity	30-60 GPa	Morgan et al. (2013) Selvadurai et al. (2005)

The rift plane was kept perpendicular to $_3$-direction, for all experiments, to encourage fracturing in the preferred orientation. A masonry drill bit was used to drill a 10 mm diameter borehole parallel to the hard way plane, up to 110 mm depth. A very slow speed of the drill press ensured minimum damage in the vicinity of the borehole. A stainless-steel pipe with the outer and inner diameter of 9 and 8 mm, respectively, was used to case the top 60 mm section of the borehole using high strength epoxy. This arrangement provided an open HF section with the length of 50 mm in the middle of the specimen (Figure 1c). The importance of a well-oriented notch has been considerably emphasized upon by many researchers, where the size and the direction of initial notch can significantly affect how the HF initiates (Lhomme et al., 2005; Sarmadivaleh et al., 2013; Savic et al., 1993). However, slight deviations in notch location with respect to the preferred fracture plane (perpendicular to $_3$), can result in fracture initiation from a point other than the pre-existing flaw (Fallahzadeh et al., 2017). Also, in the field, it is difficult to control the exact location and depth of the perforations and the damage induced by the drilling process

may also govern the initiation of the fracture (Bunger & Lecampion, 2017). Therefore, due to uncertainty in obtaining a perfectly vertical notch at a certain depth inside the small borehole in very hard Barre granite rock, the HF was performed without any initial notches. Instead, a high differential stress ($_2$- $_3$) was used to assist the initiation and propagation of fracture in the preferred direction. A high deviatoric stress ($_2$/ $_3$ = 2-3) can result in a more planar and simpler HF geometry (Maxwell et al., 2016; Pan et al., 2020). Therefore, the maximum horizontal stress ($_2$) was chosen to be 2.5 times (8.625 MPa) of the minimum horizontal stress ($_3$) (3.45 MPa).

2.2 Experimental setup

Detailed description regarding the loading and injection setup has been provided in the supplemental file (S1). During the HF experiment, the emitted AE signals were detected and recorded using 16 piezoelectric sensors (Figure 1d), at a sampling rate of 5 MHz, and connected to two eight-channel boards from the MISTRAS group. These miniature Nano-30 sensors, with a small diameter of about 8 mm, had a resonant response of 300 KHz with a frequency response over the range of 125-750 KHz. To keep the size of collected AE data manageable, hit-based triggering was used with a threshold of 50 decibels (dB) i.e. the system recorded a signal upon registering any amplitude greater than 50 dB. To assist detection, the output voltage of the AE sensors was either amplified by 20 dB or 40 dB, using 2/4/6 PAC pre-amplifiers, for different experiments. Initially the experiments for different propagation regimes were performed with 20 dB gain only. However, it was found that the AEs detected from TPR experiments were not adequate for further analysis and therefore, additional experiments with 40 dB gain were conducted to complement those with 20 dB gain setting. Using different gain for each type of experiment identified the merits and demerits of using both the high and the low gain. Goodfellow et al. (2013) utilized sensors amplified by 6 dB and 40 dB in a triaxial deformation experiment and highlighted the benefit of utilizing different amplification to retrieve the loss in ampltidue information. Perfect synchronization between the AE signals and the borehole pressure data was achieved by recording the pressure data directly in the AE system at a rate of 10 Hz. The experimental protocol adopted for the conduct of experiment has been described in the supplemental file (S2). Figure 1e presents a schematic of the complete experimental setup.

2.3 Crack Source localization and characterization through AE data processing

All the recorded AE signals were analyzed for AE event location which assisted in mapping the spatio-temporal evolution of fluid induced cracking in granite cubes. The AE event location was determined based on the first arrival of the P-waves, where the exact arrival of the P-wave was determined using the Akaike Information Criterion (AIC) (Maeda, 1985). AIC can efficiently seperate events (noise and energy motion) in the same time series and has been successfully used to determine the onset time of seismic signals (Kurz et al. 2005; Sleeman & Van Eck, 1999). In this study, AE source localization was performed by minimization of residuals following the procedure described in Li et al. (2019). The MATLAB

function “fmincon” was used to optimize the source locations determined using a constant velocity model of 4000 m/s. Each AE event must be detected by atleast 4 sensors with a maximum error tolerance of 5 mm, which is ~3% of the side length of the granite cube (165 mm), from arrivals. This location error was calculated by multiplying the P-wave velocity and the difference between the predicted and observed travel time between the sensor and determined source location. While constant velocity model was used to determine the AE source locations, the Barre granite is transversally anisotropic with different velocities in different directions and this can result in an additional error in the determined AE locations.

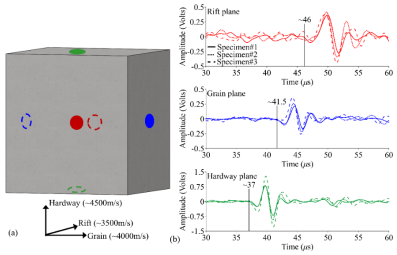

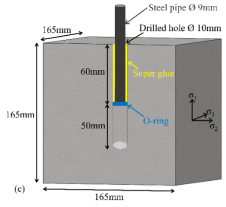

Figure 1. Specimen and borehole configuration used for the HF experiments

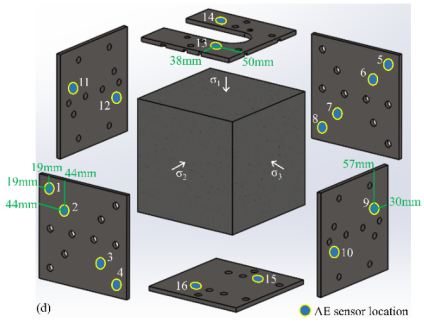

Figure 2. AE sensor locations for the HF experiments

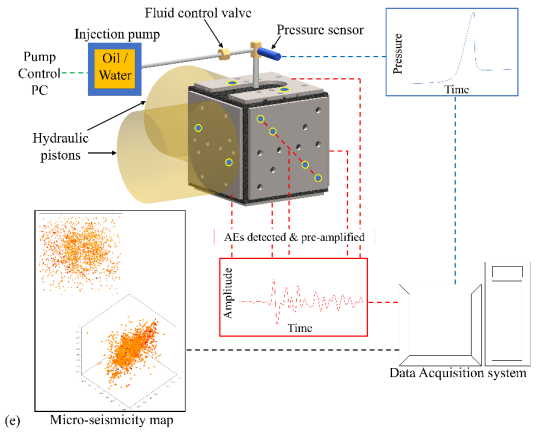

Figure 3. Schematic of the complete experimental setup

Figure 1. (a) Schematic of the cubic specimen with the position of sensors for acquiring ultrasonic waveforms (b) ultrasonic waveforms acquired along different planes for three Barre granite cubic specimens (c) Schematic of the specimen and borehole configuration used for the HF experiments. A small borehole with a radius of 5 mm was selected with respect to its distance to the boundaries of the cubic block (82.55 mm) (d) The location of 16 Nano-30 AE sensors, with an aperture of 8 mm, selected for the HF experiments providing sufficient coverage of the entire block. Eight sensors were located in the direction of fracture propagation ($_2$), and four each in the $_3$ and $_1$ directions (e) Schematic of the complete experimental setup. The data from the AE sensors were amplified and recorded in the computer for post-experiment analysis. The data from the hydraulic pistons and the pressure sensor, located 50mm above the borehole entrance, was also recorded in the same computer to achieve synchronization between the pressure, confining stress, and the AE data (not to scale)

A moment tensor is a representation of the source of a seismic event, where it describes the deformation at the source location that generates the seismic waves. A moment tensor contains the properties of a fracture and can classify each detected AE event as tensile, shear, or a mixed mode (combination of tensile and shear) (Ohtsu, 1995). In this study, a less tedious moment tensor inversion method, known as the Simplified Green's function for Moment tensor Analysis (SiGMA) was applied to the recorded AE data, as described in Ohno & Ohtsu (2010), Chang & Lee (2004), and Hampton et al. (2018). SiGMA selected only the initial portion of the detected AE signals, from a minimum of 6 sensors, for arrival time, amplitude, and polarity, to determine the six independent moment tensor components. The determined symmetric 2nd degree tensor (3x3 matrix), with six independent elements, were later decomposed into eigenvalues based on

the proportions of DC, compensated linear vector dipole (CLVD) part, and the isotropic (ISO) part. Absolute amplitudes are not required for this analysis and relative ratios of the moment tensor components were sufficient to determine the source mechanisms. The ratio of the DC contribution, was used to characterize the fracture source mechanism as shear (DC>0.6), tensile (DC<0.4), or mixed-mode (0.4<DC< 0.6) (Ohtsu, 1991).

2.4 Dimensionless toughness parameter (κ)

According to Detournay (2004), the value of dimensionless toughness parameter (κ) can ascertain if the propagation occurs in the VPR or TPR in the laboratory, depending on the time of the experiment. This is obtained using the basic HF propagation model, involving a planar crack, where the fracture propagates quasi-statically by the injection of a Newtonian fluid at a constant injection rate in opening mode being perpendicular to the minimum principal stress in an elastic medium (Detournay, 2016). This dimensionless parameter can be calculated as follows:

$$\kappa = K^{'} \left(\frac{t^2}{\prime^5 Q_o^3 E^{\prime 13}} \right)^{\frac{1}{18}} \quad (1)$$

where $K^{'} = (\frac{32}{\pi})K_{\mathrm{IC}}$, ($K_{\mathrm{IC}}$ = Mode-I fracture toughness of the rock); $E^{'} = (\frac{E}{1-v^2})$, ($E$ = Young's modulus; v = Poisson's ratio); $^{'} = 12$ (= fracturing fluid viscosity); t = fracture propagation time Q_o= Rate of fluid injection. For κ 1, the VPR dominates and for κ 3.5, the TPR dominates (Savitski and Detournay, 2002). The grain size of the host rock influences the fracture toughness and dilatancy properties and may have a more significant effect for laboratory fracturing compared to the field; however, micro-structural scaling was found to be impractical, as reported by De Pater et al. (1994a,1994b) and is not considered in the present study.

The required inputs for determination of κ are mechanical properties of the rock, the injection fluid's rate and viscosity, and the fracture propagation time. The rift (weakest) plane material properties of the Barre granite, taken from the literature, were used to determine the dominant propagation regime. Injection fluids with drastically different viscosities, water (1 cP) and SAE 85w-140 (Super Tech Co.) gear oil (1450 cP), were used for the HF experiments, where both fluids were injected at a constant injection rate of 1 ml/min. This particular gear oil was used keeping in view the highest viscosity limitation of the available injection pump. The viscosity of fluids is pressure dependent (especially gear oil), where viscosity generally increases with the increase in pressure (Schmelzer et al., 2005). However, the change in viscosities is expected to be small for the pressure ranges (15-25 MPa), the fluids will be subjected to in the current experiments (Bair, 2016; Bett & Cappi, 1965; Nakamura et al., 2016).

An important input parameter to determine the dominant propagation regime is the the fracture propagation time, which is the time from the fracture initiation to the end of fracture propagation (fracture reaching the boundaries of the specimen in laboratory experiments). It is imperative to determine this exact

period from the fracture initiation to fracture arriving at the boundaries of the laboratory specimen, as it will determine the value of κ and the corresponding state of HF. Most of the laboratory studies determine this experiment time from the borehole pressure curve alone; however, the minor changes in pressure due to fluid flow in the generated fractured may make it difficult to estimate and other supplemental techniques, like AE monitoring, can be useful in finding this time period. In this study, the fracture propagation time was determined by both the the pressurization rate and the detected AE data (see section 3.1 for more details).

3 Experimental results

3.1 Well-bore pressure decay analysis and detected AEs

The borehole pressure evolution for different propagation regimes is presented in Figure 2a and 2b. Three tests each were conducted for the VPR and TPR, where two were conducted with a gain of 20 dB and one additional experiment was with 40 dB gain. Since the time to reach BP was considerably different for different injection fluids, a reference time was calculated by subtracting the BP time (time at breakdown pressure) from the experimental time. Negative values of reference time indicate the pre-breakdown stage of the experiment while positive values indicate the post-breakdown stage. Figure 2c presents the pressure evolution against the reference time for a pair of VPR and TPR experiments (one each with 20 and 40 dB gain). Detailed results and analysis will only be presented for these experiments.

The fracture propagation time (time from initiation to fracture reaching boundaries), which is a significant parameter in determining the dominant propagation regime, was determined using the pressurization rate ($\frac{\mathrm{dP}}{\mathrm{dt}} = \frac{P_2 - P_1}{t_2 - t_1}$) and the detected AEs. Figure 3 presents the detected AEs and the cumulative AEs against the borehole pressure evolution and pressurization rate ($\frac{\mathrm{dP}}{\mathrm{dt}}$) for the VPR and TPR experiments with 20 and 40 dB gain. Fracture initiation (FI) was detected following the increase in the number of detected AEs and was detected earlier by the AE system, where no significant change in the borehole pressure with experimental time or $\frac{\mathrm{dP}}{\mathrm{dt}}$ could be observed. The fracture reaching the boundaries of the specimen (FRB) can be almost deduced from the lowest point of $\frac{\mathrm{dP}}{\mathrm{dt}}$ and a sudden reduction in the number of detected AEs to an almost constant value. Table 2 lists the determined fracture propagation times (from FI to FRB) for the VPR and TPR experiments, following the same procedure. These fracture propagation times were quite different from what could be determined through the pressure curve analysis alone (departure from linearity to a constant value after BP).

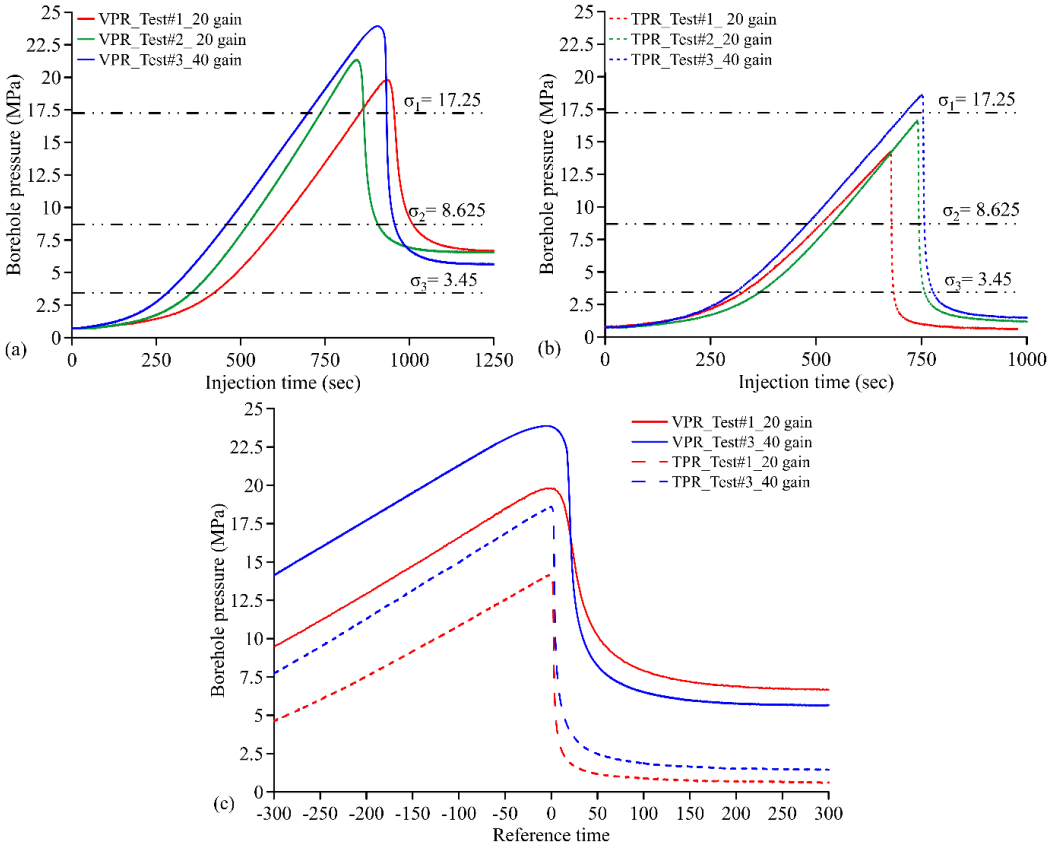

Figure 2. Borehole pressure evolution with actual experimental time for different (a) VPR and (b) TPR experiments. (c) Borehole pressure evolution against reference time for a pair of VPR and TPR experiments. On average, VPR experiments resulted in higher BPs and gradual pressure drop after the breakdown, relative to TPR experiments. For all the experiments, the borehole pressure reached a constant value after breakdown. However, this pressure was higher for VPR experiments (~6.5 MPa) as compared to the TPR experiments (~1), which represents the ease with which the injection fluid can excrete out from the generated fracture

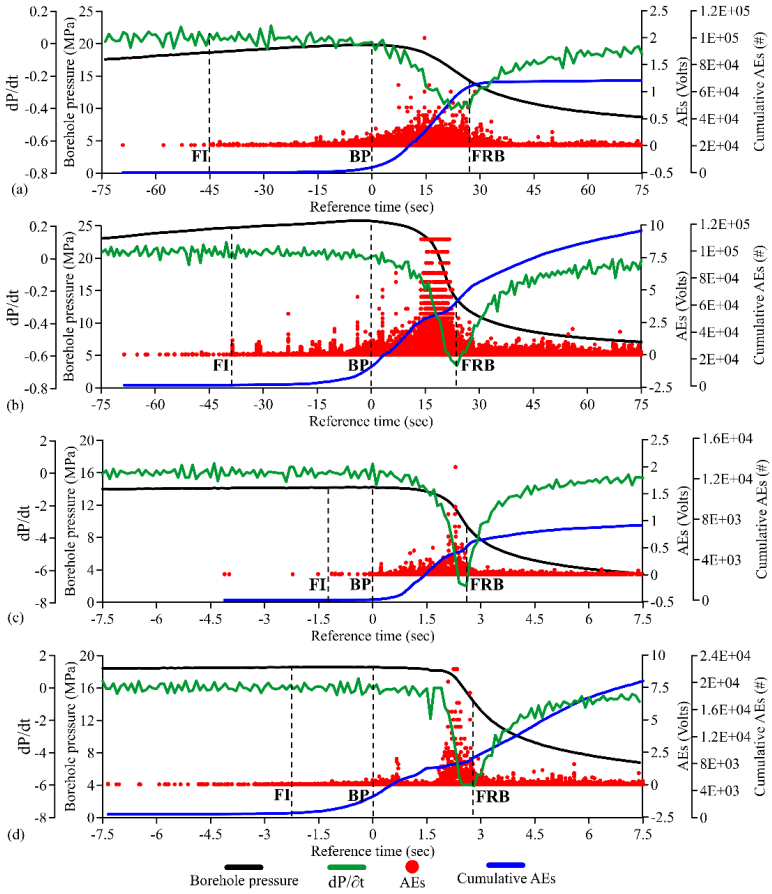

Figure 3. Detected AEs and the cumulative AEs along with the borehole pressure evolution and pressurization rate ($\frac{dP}{dt}$) against reference time for (a) VPR_Test#1_20 gain, (b) VPR_Test#3_40 gain, (c) TPR_Test#1_20 gain and (d) TPR_Test#3_40 gain; FI (fracture initiation) represents the point where the AE rate started to increase, BP (breakdown pressure) was the highest recorded borehole pressure for a particular experiment, and FRB (fracture reaching boundaries of the specimen) was determined using the pressurization rate ($\frac{dP}{dt}$) and the detected AEs. The number of AEs detected for VPR and TPR experiments, with 40 dB gain setting, were approximately 2 and 4 times higher than those detected with the 20 dB gain VPR and TPR experiments, respectively. The drop in $\frac{dP}{dt}$ for the TPR experiments were one order of magnitude higher than those of the VPR experiments

In addition, the system compliance can also have a significant impact on HF and its propagation (Ito et al., 2010). Before evaluating the different fracture propagation behavior and characteristics, it is important to determine the values of system compressibility for different dominating fracture propagation regimes.

The injection system consisted of very stiff stainless steel tubing and connectors and was identical for both VPR and TPR experiments. Therefore, system compliance mainly depends on fluid compressibility, which can be determined from the inverse of borehole pressure and injected fluid volume (Ito et al., 2006). While the viscosities of gear oil and water were drastically different, the pressurization rates (Figure 2c and Table 2) were found to be almost identical for both the VPR and TPR experiments. As both the fluids were injected at same rate (1 ml/min), this also resulted in similar values of system compressibility (C) (Table 2). These values are lower than those calculated for a stiff system in the field by Ito et al. (2006) and therefore can be representative of a system with minimum system compliance.

3.2 Determination of dominant propagation regime

The values of dimensionless toughness parameter ( ), Eq. (1), with different experimental conditions (different injection fluids, injection rates and fracture propagation times) are presented in Figure 4. Based on the different propagation times determined after the experiments, ranges of values were determined for experiments with different injection fluids performed for this study. The determined propagation regimes for different experimental conditions are presented in Table 2.

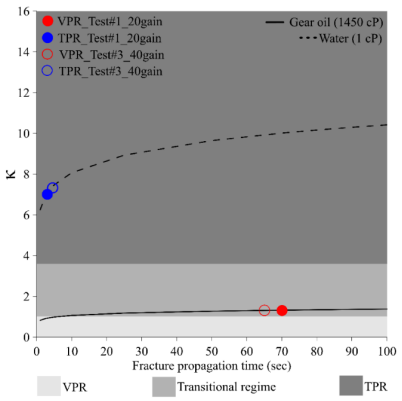

Figure 4. The evolution of dimensionless toughness parameter, , with the fracture propagation time determined for high and low viscosity injection fluids. The points highlighted in the graph indicates the determined state of the HF operation for different experiments conducted for this study. A value of 1.25 – 1.35 corresponded to an almost viscosity dominated propagation regime, whereas a value of 7.23 – 7.43 resulted in the toughness dominated propagation regime

Table 2. Experimental parameters and results for VPR and TPR experiments

Properties	VPR_Test#1_20gain	VPR_Test
Modulus of Elasticity (GPa)	30	
Mode-I fracture toughness (MPa. $(m)^{1/2}$)	1.14	
Injection fluid	SAE 85w-140 Gear oil	Water
Fluid viscosity (cP @ 20°C and 1 atm)	1450	1
Flow rate (Q_o) (ml/min)	1	
Pressurization rate (MPa/min)	2.2	2.2
Compressibility (ml/MPa)	0.46	0.46
Propagation time through pressurization rate and AE data (sec)	70	65
	1.35	1.25
Propagation regimes	~Viscosity dominated regime	Toughness

3.3 Spatiotemporal Evolution of AE events

The AE events, were used to determine the b-value for each experiment. The focal amplitude (A_o) of the AE events was determined following Zang et al. (1998) and McLaskey & Lockner (2014), assuming spherical spreading around a reference sphere of 10 mm.

$$A_O = \sqrt{\frac{1}{k}\sum_{i=1}^{k}\left(A_i\frac{r_i}{10}\right)^2} \quad (2)$$

where k is the number of sensors detected the AE event; A_i is the peak absolute amplitude determined for each detected AE recorded at the i^{th} sensor through a MATLAB code; r_i is the distance between source and the ith sensor.

The spatiotemporal evolution of AE events inside the rock specimen during the HF experiments are presented in Figures 5 and 6 for the VPR and TPR experiments, respectively. After fracture initiation, HF propagates stably and steadily till BP, which is followed by the unstable fracture propagation and a rapid decrease in the borehole pressure. In the laboratory experiments, with finite specimen dimensions, this unstable fracture propagation terminates when the fracture reaches the boundaries of the specimen. However, even after the fracture reaches the boundaries of the specimen, some residual fracturing continues till sometime after the borehole pressure reaches a constant value. Therefore, for all the experiments, the complete propagation of a HF was divided into three distinct phases: (I) initiation to breakdown, (II) breakdown to fracture reaching boundaries of the specimen, and (III) the post fracturing phase, till the end of the experiment.

For all the experiments, phase I and II consisted of small magnitude AE events and the high magnitude AE events occurred in phase II, the unstable fracture propagation stage. It can be deduced from these Figures 5 and 6 that for both VPR and TPR experiments, phases (I) and (III) of HF were better identified in the 40 dB gain experiment. The 20 dB gain setting was unable to identify the small magnitude initial AE events surrounding the borehole injection region, especially for the TPR experiment. However, the drawback of the 40 dB gain

setting was that the AE system got saturated during uncontrolled fracturing after breakdown and was only able to record the data before and after this sudden drop in the borehole pressure. Therefore, 40 dB gain experiments was unable to map the fracture propagation stage (phase-II) of HF, which can be essential to demarkate the overall stimulated rock volume. The experiment with 20 dB gain presented a better view of the extent of fracture propagation, phase (II), of HF. The size of the stimulated region could also be underestimated if determined only from the high gain setting.

3.4 Fracture mechanisms

The identification of fracture mechanisms in a HF operation can inform the hydraulic conductivity of the generated fracture and ultimately the efficiency of the stimulation operation. These damage mechanisms, classified as tensile, shear and mixed mode, along with their orientation, were determined using the MTA and are presented in Figures 7 and 8. The number of AE events for HF experiments with TPR were much lower in number and amplitude for all types of fracture mechanisms. In all the experiments, majority tensile fractures, parallel to the $_1$- $_2$ plane, were observed near the borehole and in phase I of the HF experiment. The percentage of shear and mixed-mode fracture increased in phases II and III of the HF propagation; however, tensile fracturing still remained as the dominant type for all the experiments.

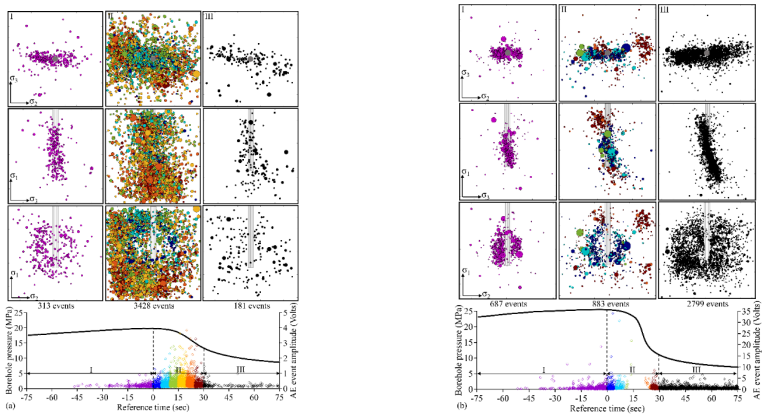

Figure 5. Spatiotemporal evolution of the AE events at different stages of the HF for (a) VPR_Test#1_20 gain, (b) VPR_Test#3_40 gain; Phase (I) initiation to breakdown, (II) breakdown to fracture reaching boundaries of the specimen, and (III) the post fracturing phase. The size of the circles represents the relative AE event amplitude in any particular experiment. The 40 db gain experiments were better at capturing the phase I and the post fracturing phase III periods.

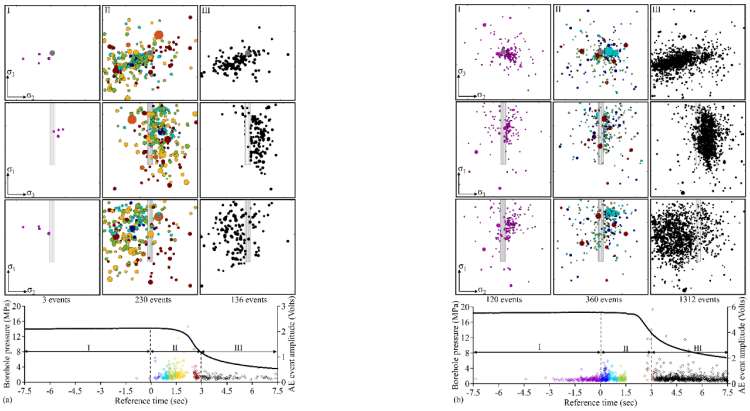

Figure 6. Spatiotemporal evolution of the AE events at different stages of the HF for (a) TPR_Test#1_20 gain, and (b) TPR_Test#3_40 gain; Only three AE events were detected during phase I of the TPR_Test#1_20_gain experiment. The HF propagated on one side of the injection borehole for both TPR experiments

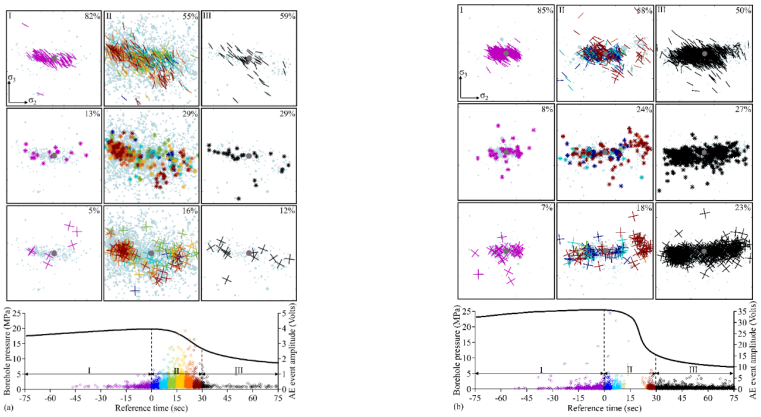

Figure 7. Crack source mechanisms determined for different phases for (a) VPR_Test#1_20 gain and (b) VPR_Test#3_40_gain experiments; tensile, mixed, and shear mode in the top, middle and bottom rows respectively. The percentage of tensile events in the initiation to breakdown phase was relatively high. However, this percentage decreased as the fracture propagated away from the borehole

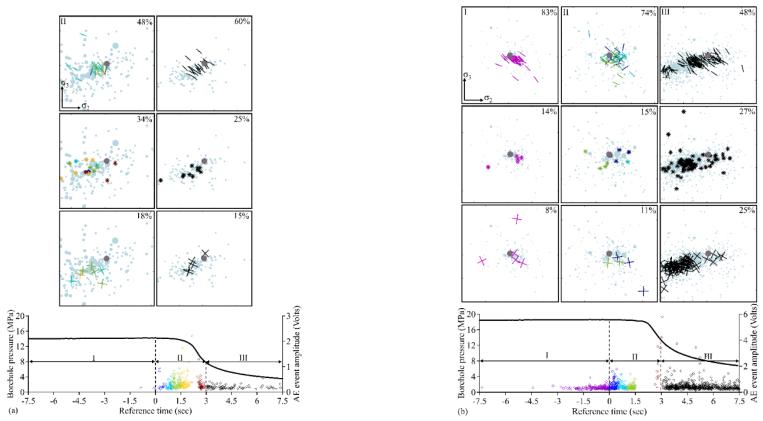

Figure 8. Crack source mechanisms determined for different phases for (a) TPR_Test#1_20 gain and (b) TPR_Test#3_40 gain experiments; tensile, mixed, and shear mode in the top, middle and bottom rows respectively. AE events were only detected in phase II and III of the 20 dB gain experiment (a), where tensile dominance near the borehole region could be observed. The absence of AE events pointed towards the saturation of the AE system and the relatively high percentage of tensile events in phase II of the 40 dB gain experiment (b).

3.5 Determination of Gutenberg-Richter b-value

The Gutenberg-Richter (GR) b-value for the frequency-magnitude distribution of the AE events determines the ratio between the large and small seismic events and is a fundamental observation in seismology and seismic risk analysis (Gutenberg & Richter, 1954). The GR distribution relates the number of seismic events (N) equal to or greater than a given magnitude, to the magnitude of the event (M), as (Gutenberg & Richter, 1942, 1944, 1956):

$$\log(N) = a - b\ M \quad (3)$$

where, a and b are constants, which depends on the seismicity rate and properties of the focal material, respectively (Olsson, 1999). A higher b-value corresponds to a higher frequency of small magnitude events, whereas a lower b-value points towards the relative abundance of higher magnitude events. In this study, b-values were calculated using the maximum likelihood method described by Aki (1965), Utsu (1965), and Woessner & Wiemer (2005):

$$b = \frac{\log_{10}(e)}{\left[<M> - \left(M_c - \frac{M_{\text{bin}}}{2}\right)\right]} \quad (4)$$

where, M_c, , and M_{bin} are the magnitude of completeness, mean magnitude, and the binning width of the seismic data, respectively. M_c is defined as the lowest magnitude at which 100% of the seismic events can be detected in space and time volume (Rydelek & Sacks, 1989; Wiemer & Wyss, 2000). In the current study, M_c was determined using Woessner & Wiemer (2005) method which

identifies the point of maximum curvature by computing the maximum value of the first derivative of the frequency-magnitude curve. This maximum curvature point, taken as M_c, is a fast estimate which has been reliably and successfully applied to natural earthquakes sequences (Gulia & Wiemer, 2019), using the slope of the logarithm of the cumulative number of the detected seismic events, i.e., $\{log\ (\Sigma\ N)\}$. For the determination of b-value, the AE event magnitude was obtained by dividing the determined focal amplitude (from Eq 2) in dB by 20, which also led to the logical selection of 0.05 as the M_{bin}. Figure 9 represents the determined b-value for both the VPR and TPR tests. The b-value for VPR and TPR experiments with 40 dB gain was calculated separately for the events before and after the gap (phase I and phase III) during the uncontrolled fracturing stage, where no AE events were detected for either of the experiment (Figure 5b and 6b). The b-values for TPR experiment with 40 dB gain was similar for both portions of AE events before and after the AE system saturation. For the VPR experiment with 40 dB gain, the b-value for initiation AE events was much lower (1.3). However, for the large portion of AE events, detected in the later phase, the b-value was found to be 1.8, much closer to the value for VPR experiment with 20 dB gain.

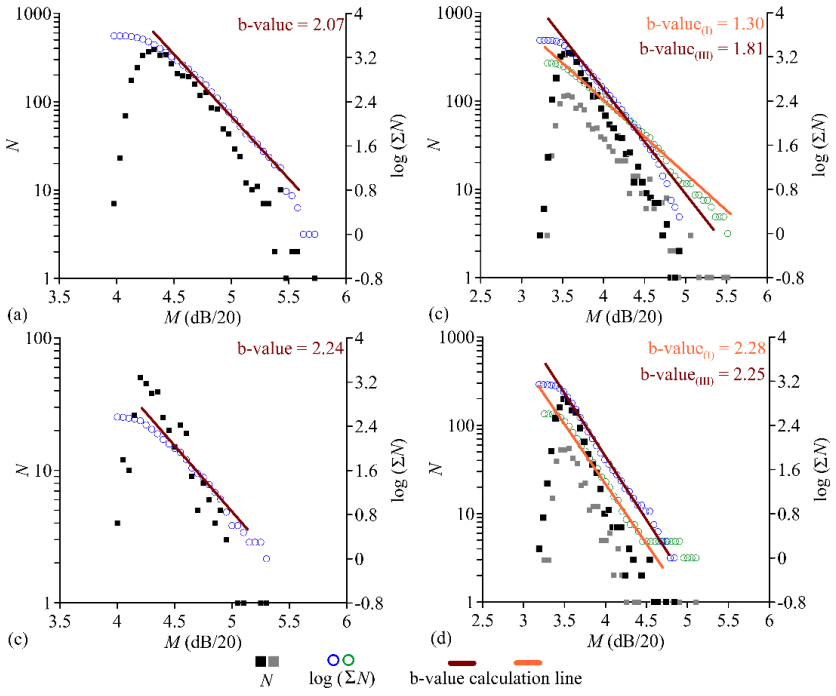

Figure 9. b-value calculation for (a) VPR_Test#1_20 gain, (b) VPR_Test#3_40

gain, (c) TPR_Test#1_20 gain, and (d) TPR_Test#3_40 gain experiments. N is the number of seismic events equal to or greater than a given magnitude (M). M was obtained by dividing the determined focal amplitude in dB by 20 and M_{bin} was selected as 0.05. The b-value was determined for the linear portion of the *log (Σ N)* and the M plot. For 40 dB gain experiments,(b) and (d), two b-values were calculated for AE events before and after the saturation of the AE system

4 Discussion

4.1 Difference in hydro-mechanical response and fracture profiles characteristics

Table 3 presents a summary of results for the VPR and TPR experiments with 20 and 40 dB gain. On average, slightly higher BP and injected volume was observed for VPR experiments, as had been similarly observed for granitic rocks with high viscosity injection fluid (e.g., Ishida et al., 2016). The injected volume till BP was calculated by multiplying constant injection rate with the time to reach the BP for a particular experiment. It can be deduced from Figures 2 and 3 that the pressure decay was abrupt for TPR experiments and the fracture propagation time was almost ten times smaller for TPR experiments relative to VPR experiments. This sudden pressure drop will result in temporary increased injection rate which represents the fluid flowing inside the generated fracture (Q_{in}). Q_{in} was calculated for the VPR_Test#1_20gain and TPR_Test#1_20gain experiments, using system compressibility (C), pressurization rate ($\frac{\text{dP}}{\text{dt}}$), constant flow rate ($Q_o$) following Eq (6) (Lecampion et al., 2017), and presented in Figure 10.

$$Q_{\text{in}} = Q_o - C \frac{\partial P}{\partial t} \quad (5)$$

Figure 10 indicates that the Q_{in} for the TPR experiment increased almost instantly to a much higher value (155 ml/min) relative to the VPR experiment (12 ml/min). This high fluid entering rate in the fracture, for the TPR experiment, can be attributed to the low viscosity of water with negligible viscous resistance relative to gear oil. These results are in line in what has been encountered by Lecampion et al. (2017) for laboratory HF experiments in the VPR and TPR using PMMA and cement blocks. In the field, it is also expected that the pressure drop and Q_{in} for the TPR experiments, conducted with low viscosity gas, will be much higher relative to the VPR experiments. For both experiments, as the fracture propagated, Q_{in} became equal to the constant injection rate.

Table 3. Summary of results for VPR and TPR experiments

@ >p(- 18) * >p(- 18) * >p(- 18) * >p(- 18) * >p(- 18) * >p(- 18) * >p(- 18) * >p(- 18) * >p(- 18) * >p(- 18) * @ Propagation regime & Test number/gain & BP

(MPa) & Injected volume till BP

(ml) & Number of AE events

(#) & Maximum amplitude of the AE event

(Volts) & b-value & Fracturing mechanisms

(%) & &
& & & & & & & Tensile &

Shear

& Mixed
VPR & 1/20dB & 19.8 & 15.6 & 3922 & 5.7 & 2.1 & 57.8 & 14.6 & 27.6
& 3/40dB & 24.5 & 15.2 & 4369 & 34 & 1.3 (I)

1.8 (III) & 59.2 & 18.4 & 22.4
TPR & 1/20dB & 16.6 & 12.1 & 369 & 2.2 & 2.2 & 57.7 & 13.8 & 28.7
& 3/40dB & 18.6 & 11.3 & 1792 & 14.1 & 2.3 (I)

2.3 (III) & 56.5 & 20.2 & 23.3

With regards to the physical characteristics of the generated HF, the fracture propagated almost symmetrically for all VPR experiments, whereas, for the TPR experiments it propagated in one direction only (Figures 5 and 6). In the field, fracture initiates and propagates near the wellbore plug, which are the zone of stress concentrations (Hampton et al., 2013), whereas in the laboratory, stress concentration occurs near the top and bottom edges of the open borehole region. For VPR experiment with 40 dB gain (Figure 5b), which better captured phase-I of fracturing, the fracture inititation occurred in almost a circular plane perpendicular to $_3$, surrounding the open injection section. For TPR experiment with 40 dB gain (Figure 6b), the fracture initiation occurred near the top edge of the injection section, which can be a zone of stress concentration. From phase-II of VPR experiment with 20 dB gain (Figure 5a), the fracture was found to be increasing in size almost as concentric circles for the VPR experiment. Comparably, for the TPR experiment (Figure 6a), the fracture propagated haphazardly on either side of the injection location. These results indicates that HF propagation for TPR situations, with much lower viscosity fluids, will be much more affected by the areas of stress concentration and local heterogeneity relative to VPR. Ishida et al. (2021) conducted a small-scale HF field experiment using CO_2 in a railroad tunnel in Japan. The fracture geometry was similar to what has been observed in the TPR experiments in this study, where fracture propagated more on one side of the injection hole relative to other. Huang et al. (2019) numerically analyzed the difference in fracture profiles for VPR and TPR conditions using discrete element modelling. For TPR settings, resulting fractures were more tortuous and assymterical with one wing being arrested, similar to the results obtained in this study for TPR experiments (Figure 6b). While in Niobrara Shale cubes, Stanchits et al. (2015) encountered similar results, where fracture propagated only in one direction for experiments involving low viscosity injection fluids.

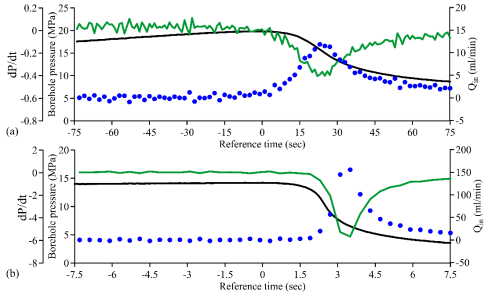

Figure 10. Flow of fluid into the fracture (Q_{in}) for (a) VPR_Test#1_20gain and (b) TPR_Test#1_20gain. Note the difference in scale of Q_{in} between VPR and TPR experiment. Q_{in} for TPR experiment was one order of magnitude higher than that of the VPR experiment.

4.2 Characteristics of microseismicity for different propagation regimes

In all the experiments of the current study, whether in the VPR or the TPR, tensile fracturing events were found to be dominating. Hampton et al. (2014) encountered similar results of about 70.5% tensile source mechanisms in HF of South Dakota granite using high viscosity gear oil. With low viscosity water, Yamamoto et al. (2019) observed very strong dominance of tensile fracturing in Kurokami–jima granite, when, similar to the current experiment, the rift (weakest) plane was orthogonal to the fracturing direction. Even in low permeability Eagle ford shale, Naoi et al. (2020) experienced similar tensile dominant fracturing with low viscosity injection fluid and concluded that fracturing mechanisms depend on the interaction of the fracturing fluid and the pre-existing microdiscontinuities. All these studies utilized MTA for the evaluation of fracture source meachanisms, which is favorable for seismic sources involving significant Non-DC component. Apart from the early tensile fracturing events dominance, the current study also highlighted how this dominance is reducing as the fracture is propagating away from the injection source. Such evolution has not been reported in previously conducted HF experimental studies. Figure 11 presents the evolution of the fracturing mechanisms from the borehole till the boundaries of the specimen in the direction of fracture propagation. The strong tensile dominance in the stable fracture initiation stage (82 – 85%) for both VPR and TPR experiments can be attributed to expansive dilation of the region surrounding the borehole due to highly pressurized fluid as reported by Schmitt & Zoback

(1992) for Westerly granite cylinders and even for Nash Point Shale by Gehne et al. (2019). Since the material has very low permeability, the fluid permeation in the material was negligible, even for the low visocisty water. This resulted in similar fracture initation behavior both for VPR and TPR experiments. During the rapid unstable fracture propagation, fracture will deviate slightly from planarity, as can be observed clearly for VPR experiment with 20 dB gain (Figure 5a), which captures the unstable fracture propagation. This along with the proximity of propagating fracture with the loading platens can contribute to HF becoming complex and results in a combination of different fracturing mechanisms as the perimeter of the HF increases. To corroborate this observation, specimens from the VPR and TPR experiments with 20dB gain were cut perpendicular to the borehole axis to observe the fractures after the HF experiments. Figure 12 presents the HF generated for the VPR and TPR experiment along with determined AE events locations. Zoomed-in segments of fractures at different distances from the injection borehole are also presented in Figure 12. It can be observed that HFs were planar with wider aperture closer relative to farther from the injection source for both the VPR and TPR experiments. As the perimeter of the HF increases, HFs becomes complex and torturous with more branches. When comparing the HF between VPR and TPR experiments, it can also be observed that overall the HF generated for the VPR experiment was relatively planar with wider aperture compared to the TPR experiment.

The b-value calculated both for the two VPR and TPR tests were close to 2, where TPR tests exhibited a slightly higher b-value relative to VPR tests (Figure 9). A b-value close to unity is normally encountered for natural earthquake sequences. However, Schorlemmer et al. (2005) have suggested that the b-value varies depending on the style of faulting, with highest b-values for normal (tensile) faulting, intermediate values for strike-slip, and lowest for thrust type events. Generally, a b-value of 2 is obtained from the seismicity induced by the main fracturing portion of the field HF operations (Maxwell et al. 2009; Downie et al. 2010. Wessels et al. (2011) observed a b-value of ~2 for seismic events generated as a result of HF in the Barnett shale formation in Ft. Worth Basin, Midcontinent USA. Eaton et al. (2014a) calculated the b-value for three different HF projects (Horn river basin, central Alberta, and Cotton valley), with different geological settings. The seismic data from the gas fields resulted in a b-value which varied from 1.63 to 2.61. In the Soultz-sous-Forêts (Alsace, France) and Basel (Switzerland) EGS projects, Cuenot et al. (2008) and Bachmann et al. (2011) obtained an overall b-value of 1.29 and 1.56, respectively. Recently, mine-scale HF experiments at the Aspo Hard Laboratory (Sweden) were carried out to evaluate the applicability of different injection schemes for EGS (Niemz et al., 2020). The cyclic progressive injection scheme resulted in higher b-values (2.34 - 2.51) relative to the conventional continuous injection schemes (1.72-1.95). The b-value determined for the experiments in current study are in line with what should be expected for HF operations. The slightly higher b-value for the TPR experiments indicates the presence of a higher number of small magnitude events which can correspond to a complex fracture network consisting of various

small fractures. This can be expected for TPR experiments in the field, which are conducted with a very low viscosity fluid (for example, CO_2), which can penetrate and activate the pre-exisitng discontinuities relatively easily and result in a complex fracture network, as compared to the VPR conditions.

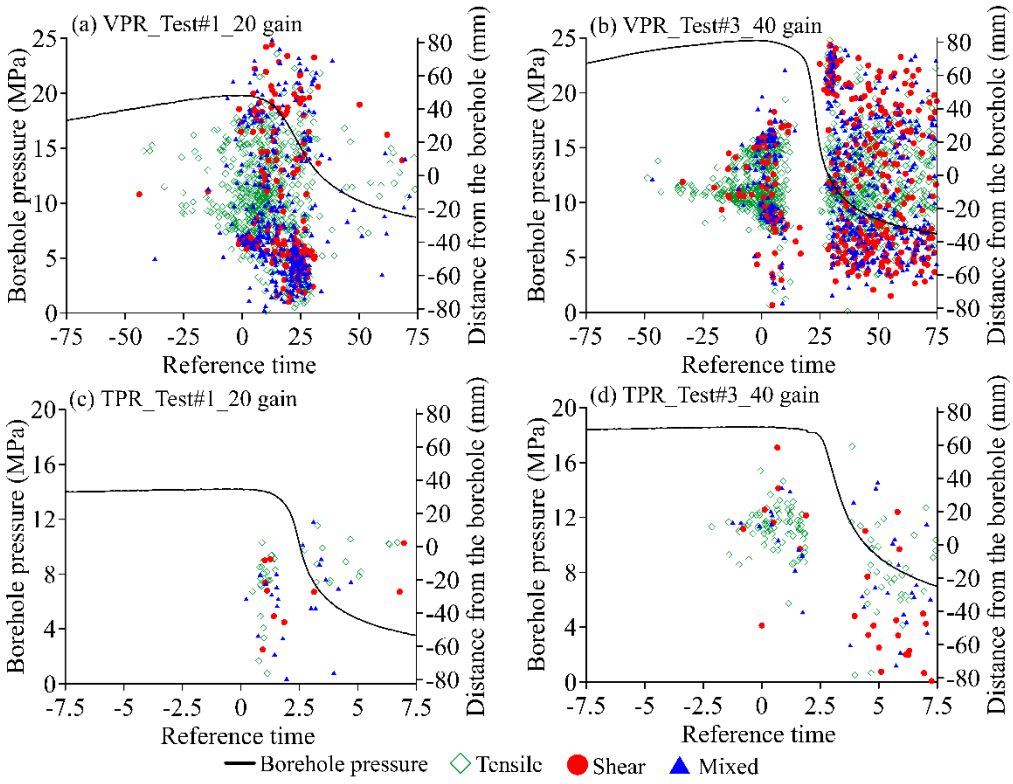

Figure 11. Damage mechanisms (tensile, shear, and mixed mode) with distance from the borehole for (a) VPR_Test#1_20 gain (b) VPR_Test#3_40 gain (c) TPR_Test#1_20 gain and (d) TPR_Test#3_40 gain. The distance is from the center (0) to the boundaries of the specimen in the direction of fracture propagation. Relatively more events were detected in the post fracturing phase by the 40 db gain experiments. The absence of events in (b) and (d) for a small period is due to the saturation of the AE system

4.3 Implications for field HF operations

Similar to the results obtained in this study, in the field it is also expected that HF stimulations with the TPR conditions, utilizing for example CO_2, will result in low BPs relative to HF with VPR as the dominant regime. This lowering of BP can be attributed to the relatively easily penetration of low viscosity injection fluid into the micro-cracks/fractures either pre-exisitng or created due to fluid pressure surrounding the injection borehole. The geometry of the generated HF is also expected to be much more complex for TPR relative

to VPR. The low visocisty injection fluid, relative to higher visocisty fluid, can activate the micro-cracks surrounding the propagating HF and will result in a more three-dimensional tortuous fracture with many secondary branches (Ishida et al. 2016).

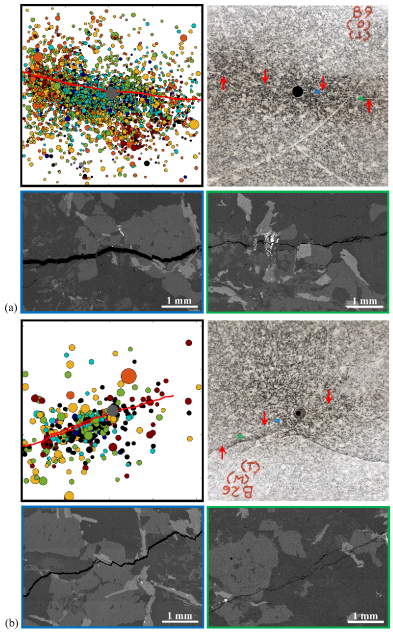

Figure 12. The determined AE events are related to the actual HF generated for the (a) VPR_Test#1_20 gain and (b) TPR_Test#1_20 gain experiments. For the images of the HF, specimen were cut at midpoint perpendicular to the fracture plane. The red line and arrows highlight the location of HF in a/c and b/d, respectively. Zoomed-in segments of HF closer (blue) and farther (green) from the injection borehole are also presented for both the experiments. HF becomes more complex and tortuous as it propagates away from the injection source.

Majority of the recorded seismic data, from large and intermediate field-scale HF operations have pointed towards shear dominated mechanisms, despite the theoretical predictions of tensile dominance (Gischig et al., 2018; Horálek et al., 2010; Maxwell, 2011, Maxwell & Cipolla, 2011). However, there are few cases which have suggested opening of new cracks (tensile) to be the dominant fracturing mode in field HF operations (Eaton et al. 2014b; Julian et al. 2010; Šílený et al. 2009). Some researchers (Jung, 2013; McClure, 2012; McClure & Horne, 2014a,b) have also argued against the pure shear stimulation supposition for the granitic rocks. They have proposed that HF in granitic rocks contains a much higher percentage of new fracturing than what is believed by the community and is actually a combination of both the tensile fractures and

shearing of pre-existing fractures. Observations from large scale HF projects, Fenton Hill EGS (Norbeck et al. 2018) and Sanford Underground Research facility (Schoenball et al. 2020), have also supported this notion of combined type fracturing. Ohtsu et al. (1991) applied MTA to microseismic events detected during a small-scale field HF test in Imaichi underground powerplant. While the number of microseismic events analyzed were small, tensile cracks were obtained first around the weak seams followed by shear cracks. Similarly, Cuenot et al. (2008), during 2000 and 2003 stimulation tests at Soultz-sous-Forêts France and Zhao et al. (2014) in the Basel EGS project, observed high Non-DC component microseismic events close to the injection well. In comparison, the Non-DC component of microseimsic events detected away from the injection source was negligible, indicating minimum effect of fluid overpressure. Ishida et al. (2019) and (2021) performed small-scale field experiments using water and very low viscosity CO_2, respectively. For both cases, which can be representative of VPR and TPR conditions, tensile events were encountered initially, closer to the injection source and were followed by abundant shear events. The early tensile dominance detected in these different studies were similar to what had been observed in the current study and can be attributed to the dilation of area close to the pressurized section. However, in all of the above quoted studies, as the fracture propagates away from the injection source, shear events were the dominant mode of fracturing. In the current study, while the percentage of shear events increased, tensile events were still the dominant fracturing mode. This discrepancy can be attributed to several factors, as discussed below:

- First, the material tested in the laboratory is mostly intact without any pre-existing faults/discontinuities. In the field, the rock mass mostly contains numerous fractures of different scales, which can significantly influence the HF propagation. In other words, the experiments performed in the laboratory with intact material represents pure HF experiments involving only new fractures, whereas in the field, it can be a combination of both HF (new fractures) and hydro-shearing (HS) of pre-exisitng faults/discontinuities.

- Another factor contributing towards the highlighted inconsistency can be related to the scale of the experiments/operations. The finite sized specimen tested in the laboratory may only be able to replicate only the near borehole phenomena. The increase in shear fractures observed in the current experiments away from the borehole might have even increased to a greater extent if the dimensions of the specimen were not limited.

- The low percentage of shear fractures detected in small-scale HF studies can also be attributed to the saturation of the microseismic or AE recording system in the uncontrolled fracturing phase, which is a major portion of HF propagation especially in the field. This AE system saturation can be frequently encountered in laboratory HF experiments (for example, Hampton et al. 2018; Naoi et al. 2019) but also sometimes in small-scale field HF studies involving brittle rock masses (Ishida et al. 2019). The

clipped amplitudes (Figure 3b) and long-duration signals that happen at or just after the BP, overwhelm the AE system and cause system saturation (phase II in Figures 5b and 6b). This is due to the superimposition of many large AEs and their reflections and can result in loss of significant quantity of microseismic data. Majority of these missing AE events are expected to be shear fractures, as they are the likely fracture mode at the failure point.

- Lastly, the extensive and very sensitive AE monitoring from all the sides of the specimen in the laboratory, is almost never possible in the field. Nolen-Hoeksema & Ruff (2001) have pointed out that limited microseismic monitoring from only one vertical monitoring well may be blind to the isotropic component of the moment tensor. This type of monitoring setup might not be able to detect the tensile portion of fracturing. Also, a significant portion of the deformation occurring during the HF stimulation is aseismic (Goodfellow et al., 2015; Villiger et al., 2020), which is also influenced by the distance of the field seismic recording setup from the propagating HF. These conditions may result in a situation where only the high energy seismic events, resulting from the interaction of propagating fractures and pre-existing faults/discontinuities, are detected by the seismic sensors, whereas the relatively low energy tensile events are left undetected.

5 Conclusions

This study focused on controlled laboratory HF of true triaxially loaded granitic rock cubes with different experimental settings. The selected experimental setting resulted in two drastically different HF propagation regimes: viscosity and toughness dominated propagation regimes, which can be representative of different HF conditions in the field. Real-time AE monitoring successfully mapped the generated, almost planar fracture capturing both the fracture initiation and propagation, until the fracture reached the specimen boundaries. The main conclusions are presented as follows:

- VPR experiments were characterized by having higher BPs and injected volume to reach the BP. Also, the released seismic energy (number of AE events and the highest-magnitude event) was found to be greater for the VPR experiments. The low viscosity of injection fluid in the TPR experiments assisted in the relatively easier stimulation of the micro-flaws in granite and consequently resulted in early breakdown of the specimen utilizing a lower volume of the injection fluid.

- The b-value of the frequency-magnitude distribution for both the VPR and TPR experiments (~2) was found to be much higher than those encountered for natural earthquakes (1). These b-values are in line with what is expected for HF operations. The b-value for TPR experiments was slightly higher than the VPR experiments. Higher b-values for the TPR experiments pointed towards the increased number of low magnitude

events and a relatively more complex fracture network.

- Overall, tensile dominated fracturing patterns were obtained for both the VPR and TPR experiments. This tensile dominance was most pronounced near the injection source and a combination of fracture types were encountered as the perimeter of the HF increased. This tensile dominance can be attributed to the minimum pre-exisitng faults/discontinuities in the intact rock specimen, limited size of the laboratory specimen, saturation of the AE monitoring system, and/or extensive laboratory monitoring of the HF operation.

The spatio-temporal evolution of the HF initiation and propagation along with the associated microseismicty can be essential to determine the permeabilty enhancement achieved throughout the stimulated reservoir volume during different stages of HF operation.The laboratory results, with much sensitive and extensive microseismic monitoring system, can provide significant information about the HF operation, which may not be available from the field. These results can have important implications in assessment of a HF operation in granite as the fracture pattern and morphology vary depending on the underlying damage mechanism and ultimately decide the permeability increase achieved through the stimulation operation.

Acknowledgments

This material is based upon work supported by the U.S. Department of Energy, Office of Basic Energy Sciences, geosciences program under Award Number DE-SC0019117.

Open Research

The raw and processed data utilized in the preparation of this research article can be accessed through the private data repository link : **https://figshare.com/s/fe52db679269ec382819**

References

Adams, J., & Rowe, C. (2013). Differentiating applications of hydraulic fracturing. In ISRM International Conference for Effective and Sustainable Hydraulic Fracturing. International Society for Rock Mechanics and Rock Engineering. http://dx.doi.org/10.5772/56114

Aki, K. (1965). Maximum likelihood estimate of b in the formula log N= a-bM and its confidence limits. Bull. Earthq. Res. Inst., Tokyo Univ., 43, 237-239.

Bachmann, C. E., Wiemer, S., Woessner, J., & Hainzl, S. (2011). Statistical analysis of the induced Basel 2006 earthquake sequence: introducing a probability-based monitoring approach for Enhanced Geothermal Systems. Geophysical Journal International, 186(2), 793-807. https://doi.org/10.1111/j.1365-246X.2011.05068.x

Bair, S. (2016). The temperature and pressure dependence of viscosity and volume for two reference liquids. Lubrication Science, 28(2), 81-95.

Bett, K. E., & Cappi, J. B. (1965). Effect of pressure on the viscosity of water. Nature, 207(4997), 620-621.

Bunger, A. P., & Lecampion, B. (2017). Four critical issues for successful hydraulic fracturing applications. Rock mechanics and engineering, (BOOK_CHAP).

Chang, S. H., & Lee, C. I. (2004). Estimation of cracking and damage mechanisms in rock under triaxial compression by moment tensor analysis of acoustic emission. International Journal of Rock Mechanics and Mining Sciences, 41(7), 1069-1086.

Cheng, Y., & Zhang, Y. (2020). Experimental Study of Fracture Propagation: The Application in Energy Mining. Energies, 13(6), 1411. https://doi.org/10.3390/en13061411

Cornet, F. H., Bérard, T., & Bourouis, S. (2007). How close to failure is a granite rock mass at a 5 km depth?. International Journal of Rock Mechanics and Mining Sciences, 44(1), 47-66. https://doi.org/10.1016/j.ijrmms.2006.04.008

Cuenot, N., Dorbath, C., & Dorbath, L. (2008). Analysis of the microseismicity induced by fluid injections at the EGS site of Soultz-sous-Forêts (Alsace, France): implications for the characterization of the geothermal reservoir properties. Pure and Applied Geophysics, 165(5), 797-828. https://doi.org/10.1007/s00024-008-0335-7

Dai, F., & Xia, K. (2010). Loading rate dependence of tensile strength anisotropy of Barre granite. Pure and applied geophysics, 167(11), 1419-1432.

Dai, F. & K.W. Xia. (2013). Laboratory measurements of the rate dependence of the fracture toughness anisotropy of Barre granite. International Journal of Rock Mechanics and Mining Sciences, 60, pp.57-65. https://doi.org/10.1016/j.ijrmms.2012.12.035

Dai, F., Xia, K., Zuo, J. P., Zhang, R., & Xu, N. W. (2013). Static and dynamic flexural strength anisotropy of Barre granite. Rock Mechanics and Rock Engineering, 46(6), 1589-1602.

De Pater, C. J., Cleary, M. P., Quinn, T. S., Barr, D. T., Johnson, D. E., & Weijers, L. (1994a). Experimental verification of dimensional analysis for hydraulic fracturing. SPE Production & Facilities, 9(04), 230-238. https://doi.org/10.2118/24994-PA

De Pater, C. J., Weijers, L., Savic, M., Wolf, K. H. A. A., Van Den Hoek, P. J., & Barr, D. T. (1994b). Experimental study of nonlinear effects in hydraulic fracture propagation (includes associated papers 29225 and 29687). SPE Production & Facilities, 9(04), 239-246. https://doi.org/10.2118/25893-PA

Detournay, E. (2004). Propagation regimes of fluid-driven fractures in impermeable rocks. International Journal of Geomechanics, 4(1), 35-45. https://doi.org/10.1061/(ASCE)1532-3641(2004)4:1(35)

Detournay, E. (2016). Mechanics of hydraulic fractures. Annual Review of Fluid Mechanics, 48, 311-339. https://doi.org/10.1146/annurev-fluid-010814-014736

Diaz, M., Jung, S. G., Zhuang, L., Kim, K. Y., Zimmermannn, G., Hofmann, H., ... & Min, K. B. (2018). Hydraulic, mechanical and seismic observations during hydraulic fracturing by cyclic injection on Pocheon granite. In ISRM International Symposium-10th Asian Rock Mechanics Symposium. OnePetro.

Downie, R. C., Kronenberger, E., & Maxwell, S. C. (2010). Using microseismic source parameters to evaluate the influence of faults on fracture treatments-A geophysical approach to interpretation. In SPE Annual Technical Conference and Exhibition. OnePetro. https://doi.org/10.2118/134772-MS

Eaton, D. W., Davidsen, J., Pedersen, P. K., & Boroumand, N. (2014a). Breakdown of the Gutenberg-Richter relation for microearthquakes induced by hydraulic fracturing: Influence of stratabound fractures. Geophysical Prospecting, 62(4-Vertical Seismic Profiling and Microseismicity Frontiers), 806-818. https://doi.org/10.1111/1365-2478.12128

Eaton, D. W., van der Baan, M., Birkelo, B., & Tary, J. B. (2014b). Scaling relations and spectral characteristics of tensile microseisms: Evidence for opening/closing cracks during hydraulic fracturing. Geophysical Journal International, 196(3), 1844-1857.

Fallahzadeh, S. H., Hossain, M. M., James Cornwell, A., & Rasouli, V. (2017). Near wellbore hydraulic fracture propagation from perforations in tight rocks: the roles of fracturing fluid viscosity and injection rate. Energies, 10(3), 359. https://doi.org/10.3390/en10030359

Gehne, S., Benson, P. M., Koor, N., Dobson, K. J., Enfield, M., & Barber, A. (2019). Seismo-mechanical response of anisotropic rocks under hydraulic fracture conditions: New experimental insights. Journal of Geophysical Research: Solid Earth, 124(9), 9562-9579.

Gischig, V. S., Doetsch, J., Maurer, H., Krietsch, H., Amann, F., Evans, K. F., ... & Giardini, D. (2018). On the link between stress field and small-scale hydraulic fracture growth in anisotropic rock derived from microseismicity. *Solid Earth*, *9*(1), 39-61.

Goodfellow, S. D., Nasseri, M. H. B., Maxwell, S. C., & Young, R. P. (2015). Hydraulic fracture energy budget: Insights from the laboratory. Geophysical Research Letters, 42(9), 3179-3187. https://doi.org/10.1002/2015GL063093

Goodfellow, S. D., Nasseri, M. H. B., Young, R. P., Flynn, J. W., & Reyes-Montes, J. M. (2013). Analysis of continuous acoustic emission waveform records from rock fracturing experiments. In 47th US Rock Mechanics/Geomechanics Symposium. OnePetro.

Graham, C. C., Stanchits, S., Main, I. G., & Dresen, G. (2010). Comparison of polarity and moment tensor inversion methods for source analysis of acoustic emission data. International journal of rock mechanics and mining sciences (Oxford, England: 1997), 47(1), 161.

Gulia, L., & Wiemer, S. (2019). Real-time discrimination of earthquake foreshocks and aftershocks. Nature, 574(7777), 193-199. https://doi.org/10.1038/s41586-019-1606-4

Gutenberg, B., & Richter, C. F. (1942). Earthquake magnitude, intensity, energy, and acceleration. Bulletin of the Seismological society of America, 32(3), 163-191. https://doi.org/10.1785/BSSA0320030163

Gutenberg, B., & Richter, C. F. (1944). Frequency of earthquakes in California. Bulletin of the Seismological society of America, 34(4), 185-188.

Gutenberg, B., & Richter, C. F. (1954). Frequency and energy of earthquakes. Seismicity of the Earth and Associated Phenomena, 17-19.

Gutenberg, B., & Richter, C. F. (1956). Earthquake magnitude, intensity, energy, and acceleration: (Second paper). Bulletin of the seismological society of America, 46(2), 105-145. https://doi.org/10.1785/BSSA0460020105

Hampton, J., Frash, L., & Gutierrez, M. (2013). Investigation of laboratory hydraulic fracture source mechanisms using acoustic emission. In 47th US Rock Mechanics/Geomechanics Symposium. American Rock Mechanics Association.

Hampton, J., Gutierrez, M., Matzar, L., Hu, D., & Frash, L. (2018). Acoustic emission characterization of microcracking in laboratory-scale hydraulic fracturing tests. Journal of Rock Mechanics and Geotechnical Engineering, 10(5), 805-817. https://doi.org/10.1016/j.jrmge.2018.03.007

Hampton, J., Hu, D., Matzar, L., & Gutierrez, M. (2014). Cumulative volumetric deformation of a hydraulic fracture using acoustic emission and micro-CT imaging. In 48th US Rock Mechanics/Geomechanics Symposium. American Rock Mechanics Association.

Horálek, J., Jechumtálová, Z., Dorbath, L., & Šílený, J. (2010). Source mechanisms of micro-earthquakes induced in a fluid injection experiment at the HDR site Soultz-sous-Forêts (Alsace) in 2003 and their temporal and spatial variations. Geophysical Journal International, 181(3), 1547-1565.

Hu, L., Ghassemi, A., Pritchett, J., & Garg, S. (2020). Characterization of laboratory-scale hydraulic fracturing for EGS. Geothermics, 83, 101706.

Huang, L., Liu, J., Zhang, F., Dontsov, E., & Damjanac, B. (2019). Exploring the influence of rock inherent heterogeneity and grain size on hydraulic fracturing using discrete element modeling. International Journal of Solids and Structures, 176, 207-220.

Inui, S., Ishida, T., Nagaya, Y., Nara, Y., Chen, Y., & Chen, Q. (2014). AE monitoring of hydraulic fracturing experiments in granite blocks using super-

critical CO2, water and viscous oil. In 48th US Rock Mechanics/Geomechanics Symposium. OnePetro.

Ishida, T. (2001). Acoustic emission monitoring of hydraulic fracturing in laboratory and field. Construction and Building Materials, 15(5-6), 283-295. https://doi.org/10.1016/S0950-0618(00)00077-5

Ishida, T., Aoyagi, K., Niwa, T., Chen, Y., Murata, S., Chen, Q., & Nakayama, Y. (2012). Acoustic emission monitoring of hydraulic fracturing laboratory experiment with supercritical and liquid CO2. Geophysical Research Letters, 39(16).

Ishida, T., Chen, Y., Bennour, Z., Yamashita, H., Inui, S., Nagaya, Y., ... & Nagano, Y. (2016). Features of CO2 fracturing deduced from acoustic emission and microscopy in laboratory experiments. Journal of Geophysical Research: Solid Earth, 121(11), 8080-8098. https://doi.org/10.1002/2016JB013365

Ishida, T., Chen, Q., Mizuta, Y., & Roegiers, J. C. (2004). Influence of fluid viscosity on the hydraulic fracturing mechanism. J. Energy Resour. Technol., 126(3), 190-200.

Ishida, T., Desaki, S., Kishimoto, Y., Naoi, M., & Fujii, H. (2021). Acoustic emission monitoring of hydraulic fracturing using carbon dioxide in a small-scale field experiment. International Journal of Rock Mechanics and Mining Sciences, 141, 104712.

Ishida, T., Fujito, W., Yamashita, H., Naoi, M., Fuji, H., Suzuki, K., & Matsui, H. (2019). Crack expansion and fracturing mode of hydraulic refracturing from acoustic emission monitoring in a small-scale field experiment. Rock Mechanics and Rock Engineering, 52(2), 543-553. https://doi.org/10.1007/s00603-018-1697-5

Ito, T., Igarashi, A., Kato, H., Ito, H., & Sano, O. (2006). Crucial effect of system compliance on the maximum stress estimation in the hydrofracturing method: Theoretical considerations and field-test verification. Earth, planets and space, 58(8), 963-971.

Ito, T., Satoh, T., & Kato, H. (2010). Deep rock stress measurement by hydraulic fracturing method taking account of system compliance effect. In ISRM International Symposium on In-Situ Rock Stress. OnePetro.

Julian, B. R., Foulger, G. R., Monastero, F. C., & Bjornstad, S. (2010). Imaging hydraulic fractures in a geothermal reservoir. Geophysical Research Letters, 37(7).

Jung, R. (2013). EGS—Goodbye or Back to the Future. In ISRM International Conference for Effective and Sustainable Hydraulic Fracturing. OnePetro.

Jung, S., Diaz, M. B., Kim, K. Y., Hofmann, H., & Zimmermann, G. (2021). Fatigue behavior of granite subjected to cyclic hydraulic fracturing and observations on pressure for fracture growth. Rock Mechanics and Rock Engineering,

54(10), 5207-5220.

King, M. S., Pettitt, W. S., Haycox, J. R., & Young, R. P. (2012). Acoustic emissions associated with the formation of fracture sets in sandstone under polyaxial stress conditions. Geophysical Prospecting, 60(1), 93-102. https://doi.org/10.1111/j.1365-2478.2011.00959.x

Kurz, J. H., Grosse, C. U., & Reinhardt, H. W. (2005). Strategies for reliable automatic onset time picking of acoustic emissions and of ultrasound signals in concrete. Ultrasonics, 43(7), 538-546.

Lecampion, B., Desroches, J., Jeffrey, R. G., & Bunger, A. P. (2017). Experiments versus theory for the initiation and propagation of radial hydraulic fractures in low-permeability materials. Journal of Geophysical Research: Solid Earth, 122(2), 1239-1263. https://doi.org/10.1002/2016JB013183

Lhomme, T., Detournay, E., & Jeffrey, R. G. (2005). Effect of fluid compressibility and borehole on the initiation and propagation of a tranverse hydraulic fracture. Strength, fracture and complexity, 3(2-4), 149-162.

Li, B. Q., da Silva, B. G., & Einstein, H. (2019). Laboratory hydraulic fracturing of granite: acoustic emission observations and interpretation. Engineering Fracture Mechanics, 209, 200-220.

Li, B. Q., & Einstein, H. H. (2019). Direct and Microseismic Observations of Hydraulic Fracturing in Barre Granite and Opalinus Clayshale. Journal of Geophysical Research: Solid Earth, 124(11), 11900-11916. https://doi.org/10.1029/2019JB018376

Lockner, D. (1993). The role of acoustic emission in the study of rock fracture. In International Journal of Rock Mechanics and Mining Sciences & Geomechanics Abstracts (Vol. 30, No. 7, pp. 883-899). Pergamon. https://doi.org/10.1016/0148-9062(93)90041-B

Maeda, N. (1985). A method for reading and checking phase times in autoprocessing system of seismic wave data. Zisin, 38, 365-379.

Mao, R., Feng, Z., Liu, Z., & Zhao, Y. (2017). Laboratory hydraulic fracturing test on large-scale pre-cracked granite specimens. Journal of Natural Gas Science and Engineering, 44, 278-286.

Maxwell, S. C. (2011). What does microseismicity tells us about hydraulic fractures?. In SEG Technical Program Expanded Abstracts 2011 (pp. 1565-1569). Society of Exploration Geophysicists. https://doi.org/10.1190/1.3627501

Maxwell, S. C. (2014). Microseismic imaging of hydraulic fracturing: Improved engineering of unconventional shale reservoirs. Society of Exploration Geophysicists.

Maxwell, S. C., & Cipolla, C. (2011). What does microseismicity tell us about hydraulic fracturing?. In SPE Annual Technical Conference and Exhibition.

OnePetro. https://doi.org/10.2118/146932-MS

Maxwell, S., Goodfellow, S., Lee, B., Mack, M., & Young, R. (2016). Acoustic-emission geomechanics characterization of laboratory hydraulic fracturing. In 2016 SEG International Exposition and Annual Meeting. OnePetro.

Maxwell, S. C., Jones, M., Parker, R., Miong, S., Leaney, S., Dorval, D., ... & Hammermaster, K. (2009). Fault activation during hydraulic fracturing. In SEG Technical Program Expanded Abstracts 2009 (pp. 1552-1556). Society of Exploration Geophysicists. https://doi.org/10.1190/1.3255145

McClure, M. W. (2012). Modeling and characterization of hydraulic stimulation and induced seismicity in geothermal and shale gas reservoirs (Doctoral dissertation). Stanford University.

McClure, M. W., & Horne, R. N. (2014a). An investigation of stimulation mechanisms in Enhanced Geothermal Systems. International Journal of Rock Mechanics and Mining Sciences, 72, 242-260. https://doi.org/10.1016/j.ijrmms.2014.07.011

McClure, M. W., & Horne, R. N. (2014b). Correlations between formation properties and induced seismicity during high pressure injection into granitic rock. Engineering geology, 175, 74-80. https://doi.org/10.1016/j.enggeo.2014.03.015

McLaskey, G. C., & Lockner, D. A. (2014). Preslip and cascade processes initiating laboratory stick slip. Journal of Geophysical Research: Solid Earth, 119(8), 6323-6336. https://doi.org/10.1002/2014JB011220

Merrill, T. W., & Schizer, D. M. (2013). The shale oil and gas revolution, hydraulic fracturing, and water contamination: a regulatory strategy. Minn. L. Rev., 98, 145.

Miller, J. T. (2008). Crack coalescence in granite (Doctoral dissertation, Massachusetts Institute of Technology).

Morgan, S. P., Johnson, C. A., & Einstein, H. H. (2013). Cracking processes in Barre granite: fracture process zones and crack coalescence. International journal of fracture, 180(2), 177-204.

Nakamura, Y., Hiraiwa, S., Suzuki, F., & Matsui, M. (2016). High-Pressure Viscosity Measurements of Polyalphaorefins at Elevated Temperature. Tribology Online, 11(2), 444-449.

Naoi, M., Chen, Y., Yamamoto, K., Morishige, Y., Imakita, K., Tsutumi, N., ... & Kitamura, S. (2020). Tensile-dominant fractures observed in hydraulic fracturing laboratory experiment using eagle ford shale. Geophysical Journal International, 222(2), 769-780. https://doi.org/10.1093/gji/ggaa183

Nasseri, M. H. B., Mohanty, B., & Young, R. P. (2006). Fracture toughness measurements and acoustic emission activity in brittle rocks. Pure and Applied Geophysics, 163(5-6), 917-945. https://doi.org/10.1007/s00024-006-0064-8

Niemz, P., Cesca, S., Heimann, S., Grigoli, F., von Specht, S., Hammer, C., ... & Dahm, T. (2020). Full-waveform-based characterization of acoustic emission activity in a mine-scale experiment: a comparison of conventional and advanced hydraulic fracturing schemes. Geophysical Journal International, 222(1), 189-206. https://doi.org/10.1093/gji/ggaa127

Nolen-Hoeksema, R. C., & Ruff, L. J. (2001). Moment tensor inversion of microseisms from the B-sand propped hydrofracture, M-site, Colorado. Tectonophysics, 336(1-4), 163-181.

Norbeck, J. H., McClure, M. W., & Horne, R. N. (2018). Field observations at the Fenton Hill enhanced geothermal system test site support mixed-mechanism stimulation. Geothermics, 74, 135-149. https://doi.org/10.1016/j.geothermics.2018.03.003

Nur, A., & Simmons, G. (1969). Stress-induced velocity anisotropy in rock: An experimental study. Journal of Geophysical Research, 74(27), 6667-6674.

Ohno, K., & Ohtsu, M. (2010). Crack classification in concrete based on acoustic emission. Construction and Building Materials, 24(12), 2339-2346.

Ohtsu, M. (1991). Simplified moment tensor analysis and unified decomposition of acoustic emission source: application to in situ hydrofracturing test. Journal of Geophysical Research: Solid Earth, 96(B4), 6211-6221.

Ohtsu, M. (1995). Acoustic emission theory for moment tensor analysis. Research in Nondestructive Evaluation, 6(3), 169-184. https://doi.org/10.1007/BF01606380

Olasolo, P., Juárez, M. C., Morales, M. P., & Liarte, I. A. (2016). Enhanced geothermal systems (EGS): A review. Renewable and Sustainable Energy Reviews, 56, 133-144.

Olsson, R. (1999). An estimation of the maximum b-value in the Gutenberg-Richter relation. Journal of Geodynamics, 27(4-5), 547-552. https://doi.org/10.1016/S0264-3707(98)00022-2

Pan, P. Z., Wu, Z. H., Yan, F., Ji, W. W., Miao, S. T., & Wang, Z. (2020). Effect of the intermediate principal stress on hydraulic fracturing in granite: an experimental study. Environmental Earth Sciences, 79(1), 10. https://doi.org/10.1007/s12665-019-8760-8

RILEM Technical Committee (Masayasu Ohtsu)**+ 81-96-3423542+ 81-96-3423507 Ohtsu@ gpo. kumamoto-u. ac. jp. (2010). Recommendation of RILEM TC 212-ACD: acoustic emission and related NDE techniques for crack detection and damage evaluation in concrete* Test method for damage qualification of reinforced concrete beams by acoustic emission. Materials and structures, 43, 1183-1186.

Rydelek, P. A., & Sacks, I. S. (1989). Testing the completeness of earthquake catalogues and the hypothesis of self-similarity. Nature, 337(6204), 251-253. https://doi.org/10.1038/337251a0

Sano, O., Kudo, Y., & Mizuta, Y. (1992). Experimental determination of elastic constants of Oshima granite, Barre granite, and Chelmsford granite. Journal of Geophysical Research: Solid Earth, 97(B3), 3367-3379. https://doi.org/10.1029/91JB02934

Sarmadivaleh, M. (2012). Experimental and numerical study of interaction of a pre-existing natural interface and an induced hydraulic fracture (Doctoral dissertation, Curtin University).

Sarmadivaleh, M., Joodi, B., Nabipour, A., & Rasouli, V. (2013). Steps to conducting a valid hydraulic-fracturing laboratory test. The APPEA Journal, 53(1), 347-354. https://doi.org/10.1071/AJ12029

Savic, M., Cockram, M. J., & Ziolkowski, A. M. (1993). Active ultrasonic monitoring of laboratory-scale hydraulic fracturing experiments: Numerical modelling vs. experiment. In Offshore Europe. Society of Petroleum Engineers. https://doi.org/10.2118/26793-MS

Savitski, A. A., & Detournay, E. (2002). Propagation of a fluid-driven penny-shaped fracture in an impermeable rock: asymptotic solutions. Int. J. Solids Structures, 39(26), 63116337. https://doi.org/10.1016/S0020-7683(02)00492-4

Schmelzer, J. W., Zanotto, E. D., & Fokin, V. M. (2005). Pressure dependence of viscosity. The Journal of chemical physics, 122(7), 074511.

Schmitt, D. R., & Zoback, M. D. (1992). Diminished pore pressure in low-porosity crystalline rock under tensional failure: Apparent strengthening by dilatancy. Journal of Geophysical Research: Solid Earth, 97(B1), 273-288.

Schoenball, M., Ajo-Franklin, J. B., Blankenship, D., Chai, C., Chakravarty, A., Dobson, P., ... & EGS Collab Team. (2020). Creation of a Mixed-Mode Fracture Network at Mesoscale Through Hydraulic Fracturing and Shear Stimulation. Journal of Geophysical Research: Solid Earth, 125(12), e2020JB019807. https://doi.org/10.1029/2020JB019807

Schorlemmer, D., Wiemer, S., & Wyss, M. (2005). Variations in earthquake-size distribution across different stress regimes. Nature, 437(7058), 539-542. https://doi.org/10.1038/nature04094

Selvadurai, A. P. S., Boulon, M. J., & Nguyen, T. S. (2005). The permeability of an intact granite. Pure and Applied Geophysics, 162(2), 373-407.

Šílený, J., Hill, D. P., Eisner, L., & Cornet, F. H. (2009). Non–double-couple mechanisms of microearthquakes induced by hydraulic fracturing. Journal of Geophysical Research: Solid Earth, 114(B8).

Sleeman, R., & Van Eck, T. (1999). Robust automatic P-phase picking: an on-line implementation in the analysis of broadband seismogram recordings. Physics of the earth and planetary interiors, 113(1-4), 265-275.

Solberg, P., Lockner, D., & Byerlee, J. D. (1980). Hydraulic fracturing in granite under geothermal conditions. In International Journal of Rock Mechanics

and Mining Sciences & Geomechanics Abstracts (Vol. 17, No. 1, pp. 25-33). Pergamon. https://doi.org/10.1016/0148-9062(80)90003-0

Stanchits, S., Burghardt, J., & Surdi, A. (2015). Hydraulic fracturing of heterogeneous rock monitored by acoustic emission. Rock Mechanics and Rock Engineering, 48(6), 2513-2527. https://doi.org/10.1007/s00603-015-0848-1

Stanchits, S., Surdi, A., Gathogo, P., Edelman, E., & Suarez-Rivera, R. (2014). Onset of hydraulic fracture initiation monitored by acoustic emission and volumetric deformation measurements. Rock Mechanics and Rock Engineering, 47(5), 1521-1532._ https://doi.org/10.1007/s00603-014-0584-y

Utsu, T. (1965). A method for determining the value of" b" in a formula log n= a-bm showing the magnitude-frequency relation for earthquakes. Geophys. Bull. Hokkaido Univ., 13, 99-103.

Villiger, L., Gischig, V. S., Doetsch, J., Krietsch, H., Dutler, N. O., Jalali, M., ... & Wiemer, S. (2020). Influence of reservoir geology on seismic response during decameter-scale hydraulic stimulations in crystalline rock. Solid Earth, 11(2), 627-655. https://doi.org/10.5194/se-11-627-2020

Wessels, S., Kratz, M., & De La Pena, A. (2011). Identifying fault activation during hydraulic stimulation in the Barnett shale: Source mechanisms, b values, and energy release analyses of microseismicity. In SEG technical program expanded abstracts 2011 (pp. 1463-1467). Society of Exploration Geophysicists. https://doi.org/10.1190/1.3627478

Wiemer, S., & Wyss, M. (2000). Minimum magnitude of completeness in earthquake catalogs: Examples from Alaska, the western United States, and Japan. Bulletin of the Seismological Society of America, 90(4), 859-869. https://doi.org/10.1785/0119990114

Woessner, J., & Wiemer, S. (2005). Assessing the quality of earthquake catalogues: Estimating the magnitude of completeness and its uncertainty. Bulletin of the Seismological Society of America, 95(2), 684-698. https://doi.org/10.1785/0120040007

Xia, K., Nasseri, M. H. B., Mohanty, B., Lu, F., Chen, R., & Luo, S. N. (2008). Effects of microstructures on dynamic compression of Barre granite. International Journal of Rock Mechanics and Mining Sciences, 45(6), 879-887.

Xie, L., Min, K. B., & Song, Y. (2015). Observations of hydraulic stimulations in seven enhanced geothermal system projects. Renewable Energy, 79, 56-65. https://doi.org/10.1016/j.renene.2014.07.044

Xing, Y., Zhang, G., Luo, T., Jiang, Y., & Ning, S. (2019). Hydraulic fracturing in high-temperature granite characterized by acoustic emission. Journal of Petroleum Science and Engineering, 178, 475-484.

Yamamoto, K., Naoi, M., Chen, Y., Nishihara, K., Yano, S., Kawakata, H., ... & Ishida, T. (2019). Moment tensor analysis of acoustic emissions induced by

laboratory-based hydraulic fracturing in granite. Geophysical Journal International, 216(3), 1507-1516. https://doi.org/10.1093/gji/ggy493

Zang, A., Christian Wagner, F., Stanchits, S., Dresen, G., Andresen, R., & Haidekker, M. A. (1998). Source analysis of acoustic emissions in Aue granite cores under symmetric and asymmetric compressive loads. Geophysical Journal International, 135(3), 1113-1130. https://doi.org/10.1046/j.1365-246X.1998.00706.x

Zang, A., & Stephansson, O. (2019). Special Issue "Hydraulic fracturing in hard rock". Rock Mechanics and Rock Engineering, 52(2), 471-473.

Zhao, P., Kühn, D., Oye, V., & Cesca, S. (2014). Evidence for tensile faulting deduced from full waveform moment tensor inversion during the stimulation of the Basel enhanced geothermal system. Geothermics, 52, 74-83. https://doi.org/10.1016/j.geothermics.2014.01.003

Zhuang, L., Kim, K. Y., Diaz, M., & Yeom, S. (2020). Evaluation of water saturation effect on mechanical properties and hydraulic fracturing behavior of granite. International Journal of Rock Mechanics and Mining Sciences, 130, 104321.

Zhuang, L., Kim, K. Y., Jung, S. G., Diaz, M., & Min, K. B. (2019a). Effect of water infiltration, injection rate and anisotropy on hydraulic fracturing behavior of granite. Rock Mechanics and Rock Engineering, 52(2), 575-589. https://doi.org/10.1007/s00603-018-1431-3

Zhuang, L., Kim, K. Y., Jung, S. G., Diaz, M., Min, K. B., Zang, A., et al. (2019b). Cyclic hydraulic fracturing of pocheon granite cores and its impact on breakdown pressure, acoustic emission amplitudes and injectivity. International Journal of Rock Mechanics and Mining Sciences, 122, 104065. https://doi.org/10.1016/j.ijrmms.2019.104065

Zhuang, L., & Zang, A. (2021). Laboratory hydraulic fracturing experiments on crystalline rock for geothermal purposes. Earth-Science Reviews, 103580. https://doi.org/10.1016/j.earscirev.2021.103580